

## Original Article

# Early assessment of irreversible electroporation ablation outcomes by analyzing MRI texture: preclinical study in an animal model of liver tumor

Aydin Eresen<sup>1,2\*</sup>, Kang Zhou<sup>1,3\*</sup>, Chong Sun<sup>1,4</sup>, Junjie Shangguan<sup>1</sup>, Bin Wang<sup>1,5</sup>, Liang Pan<sup>1,6</sup>, Su Hu<sup>1,7</sup>, Yongsheng Pang<sup>2</sup>, Zigeng Zhang<sup>2</sup>, Robert Minh Nhat Tran<sup>8</sup>, Ajeet Pal Bhatia<sup>2</sup>, Farouk Nouzi<sup>2,9</sup>, Nadine Abi-Jaoudeh<sup>2,9</sup>, Vahid Yaghmai<sup>2,9</sup>, Zhuoli Zhang<sup>1,2,9,10,11,12</sup>

<sup>1</sup>Department of Radiology, Feinberg School of Medicine, Northwestern University, Chicago, IL, USA; <sup>2</sup>Department of Radiological Sciences, University of California Irvine, Irvine, CA, USA; <sup>3</sup>Department of Radiology, Peking Union Medical College Hospital, Beijing 100000, China; <sup>4</sup>Department of Orthopedics, Affiliated Hospital of Qingdao University, Qingdao 266000, Shandong, China; <sup>5</sup>Department of General Surgery, Nanfang Hospital, Southern Medical University, Guangzhou 510000, Guangdong, China; <sup>6</sup>Department of Radiology, Third Affiliated Hospital of Suzhou University, Changzhou 213000, Jiangsu, China; <sup>7</sup>Department of Radiology, First Affiliated Hospital of Soochow University, Suzhou 215000, Jiangsu, China; <sup>8</sup>School of Biological Sciences, University of California Irvine, Irvine, CA, USA; <sup>9</sup>Chao Family Comprehensive Cancer Center, University of California Irvine, Irvine, CA, USA; <sup>10</sup>Robert H. Lurie Comprehensive Cancer Center of Northwestern University, Chicago, IL, USA; <sup>11</sup>Department of Biomedical Engineering, University of California Irvine, Irvine, CA, USA; <sup>12</sup>Department of Pathology and Laboratory Medicine, University of California Irvine, Irvine, CA, USA. \*Equal contributors.

Received April 4, 2022; Accepted June 22, 2022; Epub August 15, 2022; Published August 30, 2022

**Abstract:** Objectives: Accurate differentiation of temporary vs. permanent changes occurring following irreversible electroporation (IRE) holds immense importance for the early assessment of ablative treatment outcomes. Here, we investigated the benefits of advanced statistical learning models for an immediate evaluation of therapeutic outcomes by interpreting quantitative characteristics captured with conventional MRI. Methods: The preclinical study integrated twenty-six rabbits with anatomical and perfusion MRI data acquired with a 3T clinical MRI scanner. T1w and T2w MRI data were quantitatively analyzed, and forty-six quantitative features were computed with four feature extraction methods. The candidate key features were determined by graph clustering following the filtering-based feature selection technique, RELIEFF algorithm. Kernel-based support vector machines (SVM) and random forest (RF) classifiers interpreting quantitative features of T1w, T2w, and combination (T1w+T2w) MRI were developed for replicating the underlying characteristics of the tissues to distinguish IRE ablation regions for immediate assessment of treatment response. Accuracy, sensitivity, specificity, and area under the receiver operating characteristics curve were used to evaluate classification performance. Results: Following the analysis of quantitative variables, three features were integrated to develop a SVM classification model, while five features were utilized for generating RF classifiers. SVM classifiers demonstrated detection accuracy of 91.06%, 96.15%, and 98.04% for individual and combination MRI data, respectively. Besides, RF classifiers obtained slightly lower accuracy compared to SVM which were 95.06%, 89.40%, and 94.38% respectively. Conclusions: Quantitative models integrating structural characteristics of conventional T1w and T2w MRI data with statistical learning techniques identified IRE ablation regions allowing early assessment of treatment status.

**Keywords:** Hepatocellular carcinoma, irreversible electroporation, MRI, machine learning

## Introduction

Liver cancer is ranked as the sixth most diagnosed and fourth deadliest cancer worldwide and is expected to cause 30,520 deaths and 41,260 diagnoses in 2022 in the United States

[1]. Surgical resection and partial transplantation are preferred curative options for patients with hepatocellular carcinoma (HCC); yet, several factors, e.g., stage and location of the tumors, patient condition, and liver functions restrict the number of patients suitable for

these therapeutic approaches [2]. Hepatic tumor ablation, including radiofrequency ablation, microwave ablation, or cryoablation, has shown great promise for complete remission in patients with HCC tumors smaller than 3 cm (about 1.18 in) in diameter [3]. However, efficacy of these methods is challenged by location, size, and number of tumors due to “heat-sink” effect in which blood flow causes a cooling effect by reducing the volume of ablated tumor region located near major blood vessels [4]. Irreversible electroporation (IRE) is a non-thermal tissue ablation technique that instigates cell death within the tumor structure by preserving the extracellular matrix and inducing minimal inflammation [5]. During the IRE procedure, a high-frequency electrical current is delivered in short pulses without damaging surrounding tissues [6, 7]. Following the electroporation procedure, complete necrosis occurs in the center of the ablated region called the irreversibly electroporated (IRE) zone. In contrast, surrounding region includes viable cells due to the delivery of lower electric pulses [8]. The main clinical challenge in IRE ablation is accurately predicting the extent of irreversibly electroporated tumor (IRE zone, completely treated) and the surrounding reversibly electroporated tumor (RE zone, inadequately treated), regions that is needed to prevent local recurrence and protect normal liver parenchyma.

Advanced MRI sequences such as perfusion MRI (transcatheter intra-arterial perfusion (TRIP) MRI) sequences provide detailed intrinsic information about the tissues and demonstrate the macro scale reflection of the activities occurring at the cellular level. Yet, these imaging sequences involve complicated acquisition techniques that are sensitive to environmental changes. Also, they require nonstandard analysis approaches, challenging repeatability and restricting the number of available imaging institutions [9, 10]. Therefore, standardized techniques that depend on the analysis of reproducible MRI data are needed for the early assessment of electroporation.

With technology advancement, quantitative analysis of clinical data and characterizing tissue properties via texture-based features gained popularity for diagnosis and prognosis of diseases, prediction of genomic architecture

associated with malignancies, and evaluation of disease progression [11-14]. Descriptive features were computed to represent characteristics of the imaging data, and advanced statistical learning procedures were performed to develop an expert model by integrating select features [15]. Despite the benefits emphasized by previous investigations, there is limited data on the employment of texture-based quantitative analysis of MRI data to differentiate IRE from RE zones for early evaluation of response to IRE ablation therapy. This study investigated the potential benefits of quantitative analysis of structural MRI texture to generate multivariable models for early assessment of IRE ablation through differentiation of characteristic changes occurring on tissues with different underlying structures due to electroporation of liver and tumor tissues.

### Materials and methods

#### *Animal model and IRE ablation*

A total of twenty-eight New Zealand white rabbits were included in our study with two rabbits used for VX2 tumors growth to implant in eighteen other rabbits and the remaining eight rabbits were used for the normal liver group. These twenty-six rabbits were examined for analysis of structural changes after IRE ablation therapy. Following incubation of HCC tumor cells,  $1 \times 10^6$  tumor cells were injected into the hindlimbs of donor rabbits under anesthesia. Anesthesia was initiated with an intramuscular injection of ketamine (100 mg/kg) and xylazine (5 mg/kg) and maintained through isoflurane (2-3% in oxygen, 3 L/min). The growth pattern of the tumors was observed by anatomical MRI scans until the longest tumor diameter advanced to at least 3 cm. Following tumor size validation by an expert radiologist, donor rabbits were euthanized to collect tumor tissues, and 1 mm cube tumor fragments were implanted on the left lobes of eighteen rabbits with a biopsy needle under ultrasound guidance. The rabbits were visually monitored daily, and tumor size was assessed with MRI until reaching the longest diameter of 1 cm. The rabbits with healthy livers were held in their cage for a similar period before the IRE ablation experiments.

IRE ablation procedure was performed following exposure of the left liver lobe via mini-laparotomy under anesthesia. Two platinum-iridium

## Early detection IRE ablation response for liver tumor

**Table 1.** Magnetic resonance imaging acquisition parameters

Sequence	Repetition time	Echo time	Flip angle	Resolution	Thickness
T1w MRI	200 ms	2.93 ms	70°	0.804 mm	2 mm
T2w MRI	4 s	39 ms	150°	0.938 mm	2 mm
Perfusion MRI	2.6 ms	1.02 ms	8°	1 mm	2 mm

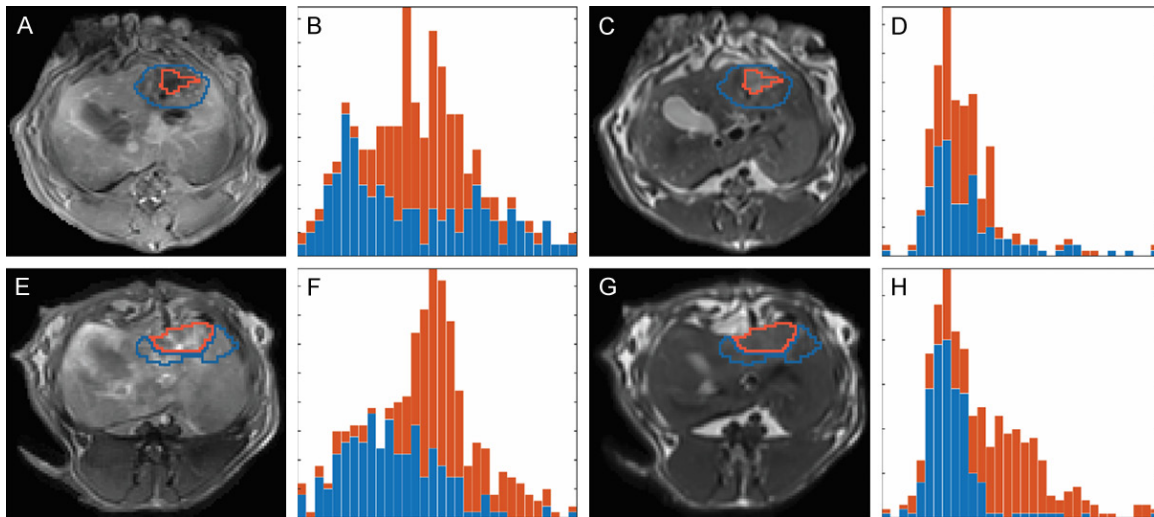


**Figure 1.** Representative MRI slices following IRE ablation to examine electroporation associated changes in diverse types of tissues (normal liver and tumor). (A) and (C) demonstrate T1w and T2w MRI of tumor tissue, and (E) and (G) illustrate T1w and T2w MRI data of normal liver following IRE ablation. The histogram plots corresponding to T1w and T2w MRI of normal liver (B and D) and tumor tissue (F and H) show the overlapping MRI intensity restricting the differentiation of ablated regions. Irreversible electroporation zone was highlighted with orange while reversible electroporation zone was marked with blue color. Note: Irreversibly electroporated tissue in orange.

electrodes were inserted at 5 mm depth of the liver tissue or tumor. Tissues were ablated using ECM830 BTX Electroporator (Harvard Apparatus, Holliston, MA) with previously reported parameters (2000 volts, 8 pulses, 0.1 ms duration, and 100 ms interval) by two experienced researchers [16, 17]. The surgery was completed by performing two-layer closure stitching, and MRI scans were completed with ongoing anesthesia with the intra-arterial administration of 3 mL of 5% gadopentetate dimeglumine solution (Magnevist; Bayer Schering Pharma, Whippany, NJ).

### MRI acquisition

MRI data were acquired via a clinical 3T Siemens Magnetom Skyra MRI scanner with anatomical (T1w and T2w MRI) and perfusion MRI (TRIP MRI) sequences described in **Table 1** following the IRE ablation procedure. In our institution, TRIP MRI was extensively studied for various research projects, and acquisition and processing guidelines were prepared with

the experience of the research personnel. During our study, perfusion characteristics of the liver and tumor tissues were examined with TRIP MRI to determine IRE ablation regions by interpreting underlying structural changes in the tissues. However, conventional T1w and T2w MRI data were analyzed to distinguish IRE ablation regions to improve reproducibility and repeatability at different institutions [16, 17]. With the consensus of two experienced radiologists under the guidance of a senior radiologist, IRE ablation regions were outlined using ITK-SNAP (v3.8), and these mask images were applied to morphological MRI data for post-procedure experiments. A representative set of T1w and T2w MRI and ablation regions following the IRE treatment procedure is presented in **Figure 1**.

### Feature extraction and selection

The intensity of MRI is relative; therefore, it should be standardized to generate a uniform scale for images acquired from different sub-

jects. A fixed-bin size quantization approach was performed to reduce these effects while empirically detecting optimal bin size among four, eight, sixteen, and thirty-two levels of details [18]. IRE ablation regions were portrayed by interpreting the behavior of intensity distribution (six first-order statistics features) and texture components (nine co-occurrence matrix (CM) features, thirteen run-length matrix (RLM) features, thirteen size-zone matrix (SZM) features, and five neighborhood gray-tone difference matrix (TDM) features) [19]. CM and RLM features were calculated in four directions and averaged to merge into a single vector. The variables were translated to zero mean and one standard deviation by performing min-max normalization. The complete list of the quantitative imaging features was introduced within [Supplementary Table 1](#).

The quantitative variables were analyzed with a two-step feature selection procedure to identify representative characteristic predictors. Initially, the pairwise correlation of the features was computed via Pearson correlation coefficient, and features were clustered depending on their similarity (**Figure 2A-C**). After evaluation of the correlation of the features within each cluster, representative features were determined for each group (**Figure 2D-F**). The importance of the candidate variables was calculated by performing a filter-based feature selection technique, RELIEFF algorithm, which interprets the interaction between quantitative MRI features and tissue characteristics through ten nearest neighbors (**Figure 2G-I**) [20]. Afterward, ten features with the highest weights were selected while optimizing and developing machine learning models.

### *Statistical analysis*

To characterize the biological effects of IRE ablation treatment, candidate quantitative features were integrated to develop a decision support mechanism via support vector machines (SVM) and random forest (RF) machine learning techniques. A total of three models were generated by analyzing quantitative features extracted from fifty-two images: T1w, T2w, and a combination of T1w and T2w MRI. The number of predictors within the model was restricted to five to prevent learning bias associated with model complexity and sample size.

As classification models were built, a search optimization approach was followed to determine the optimal combination of quantitative imaging features for obtaining robust prediction performance. Throughout the experiments, training was performed using the data by excluding an individual sample for testing the model performance and repeating until all the data was utilized for training and testing the model. Accuracy, specificity, sensitivity, and area under receiver operating characteristics curve metrics were measured for the assessment of the classification model performance. Delong method was utilized to compare significant differences in the models in terms of AUC.  $P < 0.05$  was assumed to be significant in evaluating the statistical difference of the variables. All the analyses were accomplished using either pre-defined or in-house developed scripts using MATLAB® v9.8 (MathWorks, Natick, MA).

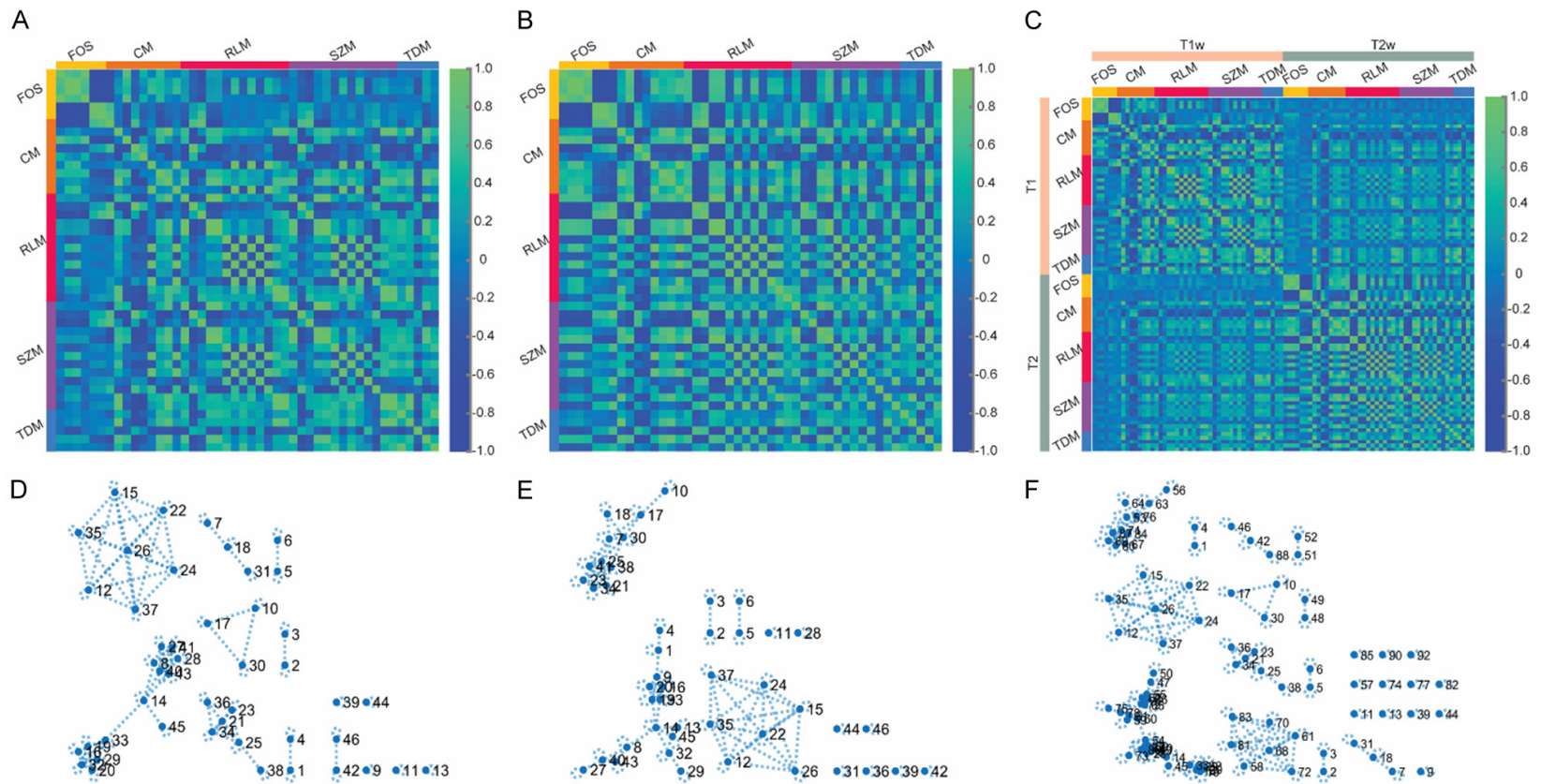
## Results

### *Feature extraction and selection*

The quantitative predictors of the conventional MRI data were examined through a two-step feature selection procedure. At first, variables were clustered through analysis of pairwise correlation (**Figure 2A-C**) that resulted in 19, 20, and 36 feature groups for T1w, T2w, and combination MRI data (**Figure 2D-F**). For T1w MRI data, seven SZM, five RLM, two-TDM, one CM, and four statistical order features were identified as representative variables. Throughout the analysis of T2w MRI data, in addition to kurtosis, nine SZM, four RLM, three CM, and three TDM features were determined as candidate variables. Four intensity distribution and fourteen texture features of T1w MRI, and one intensity distribution and seventeen texture features of T2w MRI were selected as representative variables.

The relative importance of the features was computed using RELIEFF algorithm and ten features were further examined while developing classification models. For T1w MRI data, five SZM, three RLM features, kurtosis, and busyness of TDM were included while three TDM, three SZM, three RLM features, and kurtosis were investigated during the experiments with T2w MRI for portraying the characteristic structure of ablated tissues. Two RLM, two SZM

Early detection IRE ablation response for liver tumor



## Early detection IRE ablation response for liver tumor

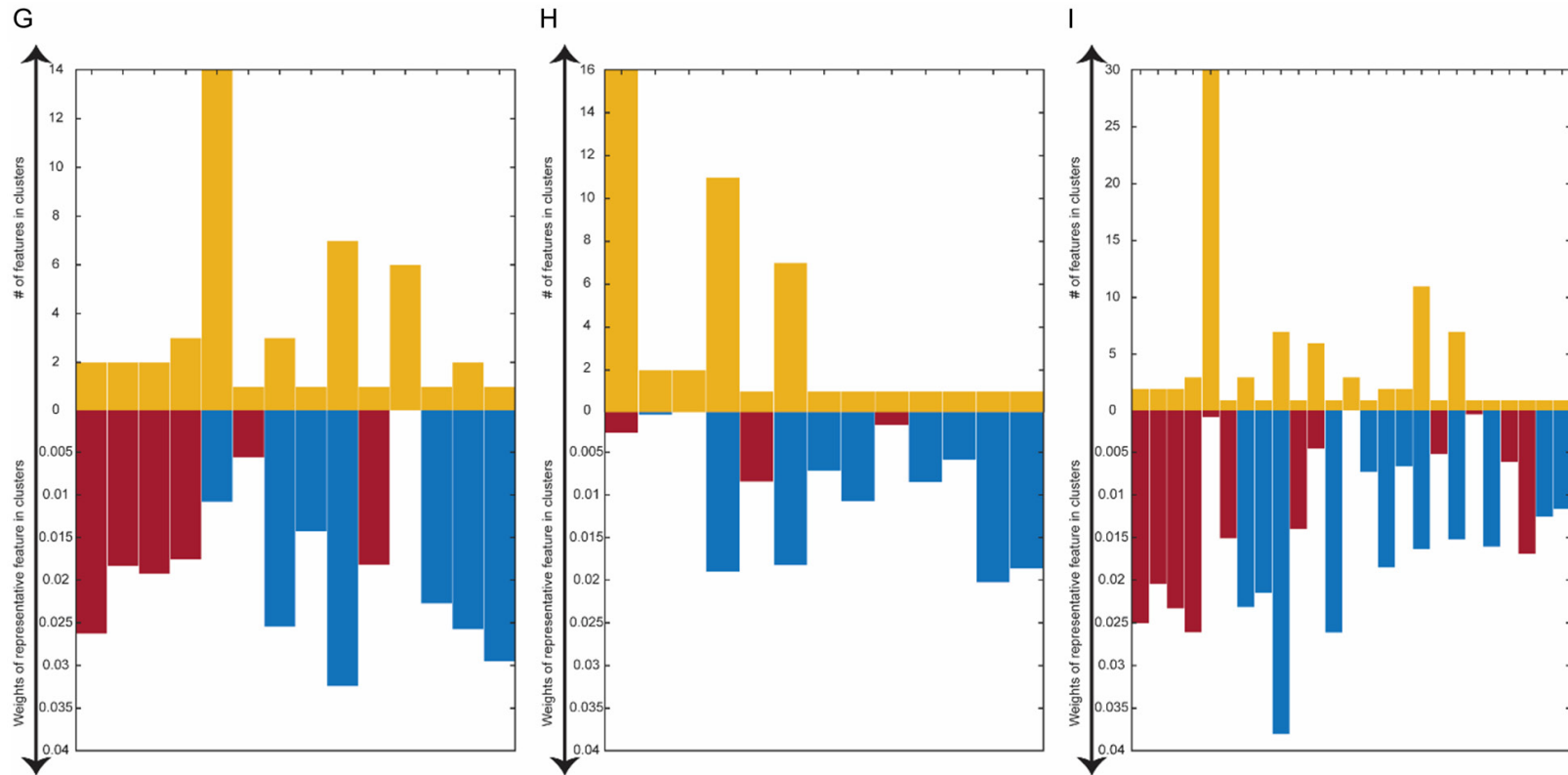


**Figure 2.** Multi-step feature selection framework for individual and combination MRI data. The interrelation of the features extracted using five different methods was demonstrated in (A-C). The graph diagram for the feature clusters is shown in (D-F). The number of features and importance of the representative features of the clusters were visualized in (G-I). FOS, first-order statistics features; CM, co-occurrence matrix features; RLM, run-length matrix features; SZM, size-zone matrix features; and TDM, neighborhood gray-tone difference matrix features.

## Early detection IRE ablation response for liver tumor

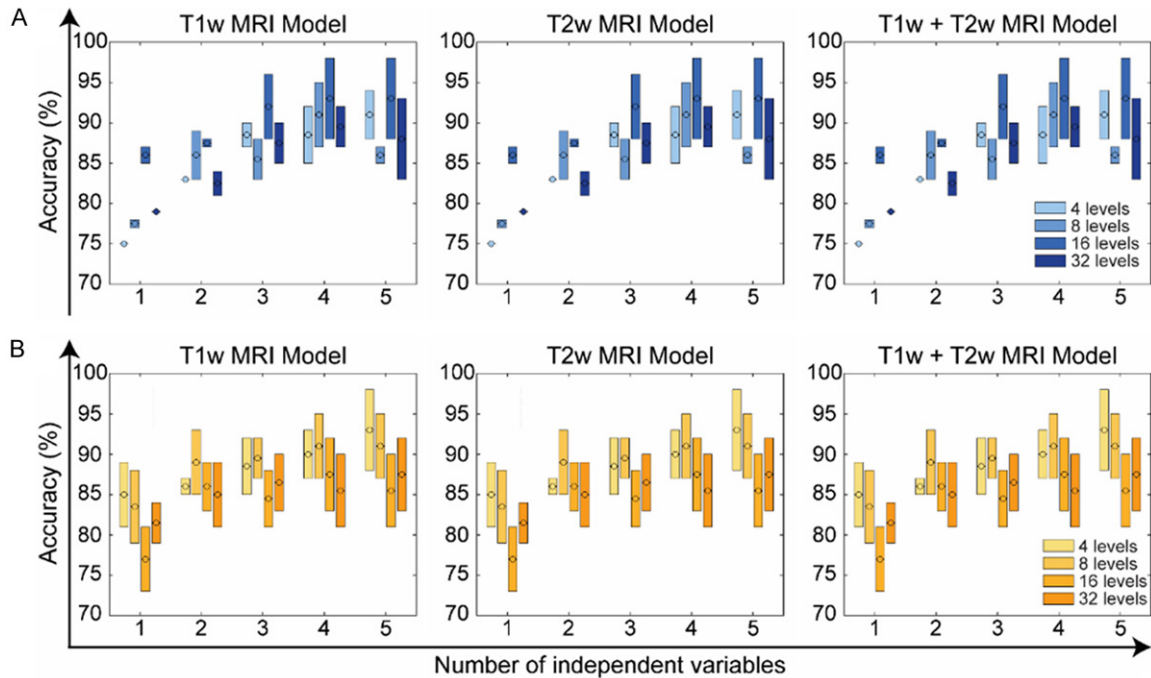


**Figure 3.** The performance of the classification models generated using kernel-based support vector machines (A) and random forest techniques (B). The increasing complexity of the classification models improved the accuracy yet affected the variation of model performance with details of image level.

features, and busyness of TDM features were computed from T1w MRI, and two SZM, two TDM features, gray-level nonuniformity of RLM, and busyness of TDM features were extracted from T2w MRI. These features were included for optimizing experiments for combination MRI model. The list of the candidate features is presented in [Supplementary Table 2](#).

### Assessment of classification models

The set of key imaging features was determined through a comprehensive analysis of the model performance while developing classification models integrating up to five combined variables computed at various levels of intensities (**Figure 3**). The classification models to distinguish irreversibly and reversibly electroporated zones following IRE ablation were developed by feeding the SVM model with three features of MRI with sixteen quantization levels, while RF models included five features of MRI data sampled with eight levels. T1w SVM classifier that interprets small zone high gray-level emphasis of SZM, long-run emphasis, and run-length variance of RLM obtained an accuracy of 91.06% for training and 82.69% for validation experiments. Additionally, the model had a sensitivity

of 92.38% and 88.46%, and a specificity of 88.46%, and 89.74% for training and validation sets, respectively. The classifier developed by combining busyness of TDM, gray-level nonuniformity of SZM, and RLM of T2w MRI demonstrated an accuracy of 96.15% for training and 88.46% for validation. The classifier obtained a sensitivity of 100% and 88.46% in addition to the specificity of 88.46% and 92.31% for training and validation trials. On the other hand, the classification model built with features extracted from T1w (long-run high gray-level emphasis of RLM) and T2w MRI data (zone-size variance of SZM and kurtosis) had improved performance compared to individual MRI models. The classifier obtained an accuracy of 98.04% and 92.31%, a sensitivity of 98.31% and 100%, and a specificity of 92.31% and 96.08% for training and validation sets. The AUC of the classification models (**Figure 4A**) were measured as 0.986, 0.941, and 0.983 for individual and combination MRI models. Random forest (RF) classification model that included five predictors has obtained stronger predictive power than classifiers interpreting features of individual MRI data (**Figure 4B**). SVM classifiers showed less variation in terms of model performance throughout the cross-validation proce-

## Early detection IRE ablation response for liver tumor

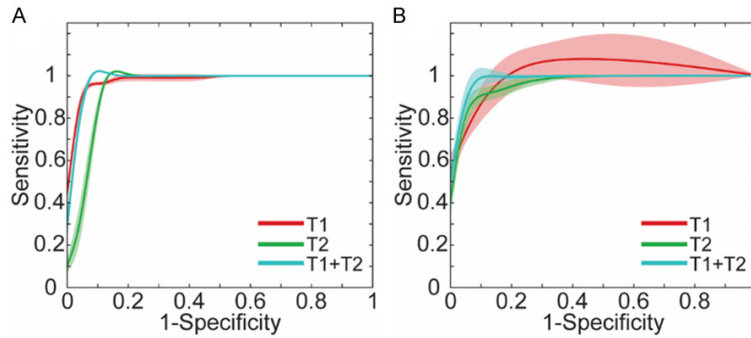


**Figure 4.** The receiver operating characteristics curve of the final classification models represents the characteristic performance of the mono and combination MRI models. Support vector machine (SVM) classifier generated with three features of combination MRI data demonstrated slightly better performance compared to classification models integrated with three features of T1w and T2w, respectively (A). Correspondingly, random forest (RF) classification model that included five predictors obtained stronger predictive power than classifiers interpreting features of individual MRI data (B). SVM classifiers showed less variation in terms of model performance throughout the cross-validation procedure than RF models which supported the superiority of the SVM classifiers compared to RF model outcome.

ture than RF models which supported the superiority of the SVM classifiers compared to RF model outcome.

RF classification models demonstrated similar performance to SVM while distinguishing reversibly and irreversibly electroporated tissue regions. The classifier integrating five features of T1w MRI data reached an accuracy of 95.06% for training and 86.54% for validation experiments. The model also had a sensitivity of 90.86% and 73.08% and specificity of 73.08% and 99.25% for training and validation. On the other hand, T2w MRI model was generated by involving gray-level nonuniformity and long-run high gray-level emphasis of RLM, busyness, and coarseness of TDM and kurtosis. It obtained 89.41% and 80.77% accuracy, a sensitivity of 91.54% and 84.62%, and a specificity of 84.62% and 87.24% for training and validation. The combination prediction model consists of three features extracted from T1w (long-run high gray-level emphasis of RLM, large zone low gray-level emphasis of SZM, and busyness of TDM) and two features of T2w MRI data (busyness of TDM and kurtosis), with an accuracy of 94.34% for training and 84.62% for validation. Moreover, the model had a sensitivity of 95.17% and 84.62%, and a specificity of 84.62% and 93.58% for training and validation. AUC values of the models (**Figure 4B**) were measured as 0.994, 0.972,

and 0.990 for single and combinatory MRI models.

### Discussion

In this study, we developed advanced statistical learning models by interpreting texture characteristics of conventional MRI data to determine biological changes following IRE ablation for early assessment of therapeutic outcomes. The classification model integrating quantitative MRI features of electroporated tissues accurately distinguished completely and partially ablated tumor or liver regions. The results showed that characteristic changes captured with perfusion imaging occurring due to IRE ablation treatment are

identified by developing a generalized statistical learning model that adopts quantitative features reflecting underlying components on a macroscale.

IRE ablation therapy holds great promise for patients with surgically unresectable solid tumors with superiority over thermal ablation techniques, e.g., safe application near arteries, minimal damage to surrounding regions, and facilitation of immune anti-tumor response [16, 20, 21]. Moreover, the permeability of the cell membranes is increased temporarily or permanently, allowing for the introduction of therapeutic molecules in the tumor cells for enhanced therapeutic efficacy. Previous studies have utilized various noninvasive imaging techniques e.g., CT [22-24], US [25-27], PET [28, 29], and MRI [16, 17] to investigate post-IRE ablation changes and differentiate permanent (IRE) and temporary (RE) ablation regions. Moreover, the safety and feasibility characteristics of the IRE ablation therapy have been demonstrated in small and large animal models [21]. Guo et al. investigated the mid-term effects of IRE ablation using a rat model of HCC [30]. The animal study demonstrated the promising advantages of IRE ablation treatment. Furthermore, long-term effects of IRE ablation have been studied through a murine model of colorectal cancer liver metastasis by another research group [31]. The results demonstrated

that IRE ablation improved the overall survival length of the mice in the treatment group significantly and increased tumor necrosis.

Throughout the last decade, revealing hidden characteristics via texture analysis has been a focus of interpretation of underlying biological variability to describe tissue classification using medical imaging data [32, 33]. The earlier studies involving quantitative image texture analysis demonstrated successful implementation of statistical learning models for disease diagnosis and prognosis, assessment of therapeutic response, genomic signature prediction, classification of tumor types, and prediction of overall survival [34, 35]. However, the characterization of IRE ablation regions through the integration of quantitative texture features and statistical learning models has not been well investigated. In this present study, the underlying structure of the tissues post-IRE ablation was examined to develop a learning framework for the early assessment of therapeutic response. Throughout the quantitative analysis of standard T1w and T2w MRI data, key imaging features were utilized to develop a classification model by employing two well-established machine learning techniques for recognizing the underlying cellular level alterations. While classification models developed with kernel-based SVM techniques obtained the best performance by interpreting three imaging features, RF classifiers included five features to reach their highest performance. SVM classifiers demonstrated more robust results than RF classifiers for our dataset in terms of generalization. For both approaches, combination models acquired slightly better accuracy, improving specificity and sensitivity for training and validation experiments. The SVM classifier of the combination MRI showed comparatively better accuracy than RF models by obtaining 98.04% for training and 92.31% for validation. The overall results demonstrated that underlying functional changes of the tissues following electroporation captured with structural MRI data can be interpreted to identify IRE vs RE ablation zones immediately after the procedure. It will enable dynamic monitoring of the therapeutic response, adjustment of IRE parameters, and modifications to treatment plans for better overall survival of patients with solid tumors.

Several limitations were present in our study. Due to the nature of the preclinical studies, the experiments were accomplished within the same environment at a single institution. The study emphasized the utilization of standard T1w and T2w MRI data with a widely available clinical 3T MRI scanner which will further allow replication of this study in all institutions performing IRE ablation therapy. Moreover, our study has identified the characteristics of the IRE ablation regions in the different types of tissues demonstrating the ability of the developed classification models to distinguish ablated regions. In these experiments, the sample size was smaller compared to clinical studies yet superior to preclinical studies focusing on therapeutic response. Our study employed machine learning models to handle smaller sample sizes, resulting in a robust and reliable outcome. Future studies with larger patient cohorts may allow the utilization of data-driven deep learning techniques to advantage autonomous image characterization.

In conclusion, the present study investigated the benefits of texture analysis for differentiation of IRE ablation vs. RE ablation regions immediately after therapy. The advanced statistical learning model integrating the quantitative features of the structural MRI data identified underlying characteristics of the tissues following the IRE ablation procedure. The results demonstrated that quantitative assessment by conventional MRI data enables noninvasive early evaluation of the IRE ablation response.

### Acknowledgements

Research reported in this publication was supported by the National Cancer Institute of the National Institutes of Health under award numbers R01CA196967, R01CA209886, R01CA241532 and P30CA062203, Society of Interventional Radiology Foundation Pilot Grant (PR-0000000012), 2019 Harold E. Eisenberg Foundation Scholar Award, and University of California Irvine Anti-Cancer Challenge Pilot Program. The content is solely the responsibility of the authors and does not necessarily represent the official views of the National Institutes of Health.

**Disclosure of conflict of interest**

None.

**Address correspondence to:** Vahid Yaghmai, Department of Radiological Sciences, School of Medicine, University of California, Irvine, 101 City Drive South, Orange, CA 92868, USA. Tel: (714) 456-6921; E-mail: vyaghmai@hs.uci.edu; Zhuoli Zhang, Department of Radiological Sciences, School of Medicine, University of California, Irvine, 839 Health Sciences Rd, Irvine, CA 92617, USA. Tel: (949) 824-5886; E-mail: zhuoliz1@hs.uci.edu

**References**

[1] Siegel RL, Miller KD, Fuchs HE and Jemal A. Cancer statistics, 2022. *CA Cancer J Clin* 2022; 72: 7-33.

[2] Belghiti J and Kianmanesh R. Surgical treatment of hepatocellular carcinoma. *HPB (Oxford)* 2005; 7: 42-49.

[3] Ryan MJ, Willatt J, Majdalany BS, Kielar AZ, Chong S, Ruma JA and Pandya A. Ablation techniques for primary and metastatic liver tumors. *World J Hepatol* 2016; 8: 191-199.

[4] Aycock KN and Davalo RV. Irreversible electroporation: background, theory, and review of recent developments in clinical oncology. *Bioelectricity* 2019; 1: 214-234.

[5] Lavee J, Onik G, Mikus P and Rubinsky B. A novel nonthermal energy source for surgical epicardial atrial ablation: irreversible electroporation. *Heart Surg Forum* 2007; 10: E162-167.

[6] Dollinger M, Zeman F, Niessen C, Lang SA, Beyer LP, Müller M, Stroszczyński C and Wiggermann P. Bile duct injury after irreversible electroporation of hepatic malignancies: Evaluation of MR imaging findings and laboratory values. *J Vasc Interv Radiol* 2016; 27: 96-103.

[7] Rubinsky B, Onik G and Mikus P. Irreversible electroporation: a new ablation modality-clinical implications. *Technol Cancer Res Treat* 2007; 6: 37-48.

[8] Scheffer HJ, Nielsen K, de Jong MC, van Tilborg AA, Vieveen JM, Bouwman AR, Meijer S, van Kuijk C, van den Tol PM and Meijerink MR. Irreversible electroporation for nonthermal tumor ablation in the clinical setting: a systematic review of safety and efficacy. *J Vasc Interv Radiol* 2014; 25: 997-1011.

[9] Papoulas M, Abdul-Hamid S, Peddu P, Cotoi C, Heaton N and Menon K. Irreversible electroporation in borderline resectable pancreatic adenocarcinoma for margin accentuation. *J Surg Case Rep* 2018; 2018: rjy127.

[10] Shangguan AJ, Zhou K, Yang J, Eresen A, Wang B, Sun C, Pan L, Hu S, Khan AT, Mouli SK, Yagh-

mai V and Zhang Z. Intra-procedural transcatheter intraarterial perfusion (TRIP)-MRI for evaluation of irreversible electroporation therapy response in a rabbit liver tumor model. *Clin Exp Gastroenterol* 2020; 13: 543-553.

[11] Huang X, Long L, Wei J, Li Y, Xia Y, Zuo P and Chai X. Radiomics for diagnosis of dual-phenotype hepatocellular carcinoma using Gd-EOB-DTPA-enhanced MRI and patient prognosis. *J Cancer Res Clin Oncol* 2019; 145: 2995-3003.

[12] Eresen A, Yang J, Shangguan J, Li Y, Hu S, Sun C, Velichko Y, Yaghmai V, Benson AB and Zhang Z. MRI radiomics for early prediction of response to vaccine therapy in a transgenic mouse model of pancreatic ductal adenocarcinoma. *J Transl Med* 2020; 18: 61.

[13] Li K, Xiao J, Yang J, Li M, Xiong X, Nian Y, Qiao L, Wang H, Eresen A, Zhang Z, Hu X, Wang J and Chen W. Association of radiomic imaging features and gene expression profile as prognostic factors in pancreatic ductal adenocarcinoma. *Am J Transl Res* 2019; 11: 4491-4499.

[14] Nie P, Yang G, Guo J, Chen J, Li X, Ji Q, Wu J, Cui J and Xu W. A CT-based radiomics nomogram for differentiation of focal nodular hyperplasia from hepatocellular carcinoma in the non-cirrhotic liver. *Cancer Imaging* 2020; 20: 20.

[15] Wakabayashi T, Ouhmich F, Gonzalez-Cabrera C, Felli E, Saviano A, Agnus V, Savadjiev P, Baumert TF, Pessaux P, Marescaux J and Gallix B. Radiomics in hepatocellular carcinoma: a quantitative review. *Hepatol Int* 2019; 13: 546-559.

[16] Figini M, Zhou K, Pan L, Sun C, Wang B, Hu S, Yang J, Shangguan J, Eresen A, Velichko Y, Yaghmai V and Zhang Z. Transcatheter intraarterial perfusion (TRIP)-MRI biomarkers help detect immediate response to irreversible electroporation of rabbit VX2 liver tumor. *Magn Reson Med* 2020; 84: 365-374.

[17] Pan L, Sun C, Zhou K, Figini M, Wang B, Shangguan J, Hu S, Yang J, Xing W, Wang J, Velichko Y, Yaghmai V and Zhang Z. Transcatheter intraarterial perfusion MRI approaches to differentiate reversibly electroporated penumbra from irreversibly electroporated zones in rabbit liver. *Acad Rad* 2020; 27: 1727-1733.

[18] Eresen A, Yang J, Shangguan J, Benson AB, Yaghmai V and Zhang Z. Detection of immunotherapeutic response in a transgenic mouse model of pancreatic ductal adenocarcinoma using multiparametric MRI radiomics: a preliminary investigation. *Acad Rad* 2020; 28: e147-e154.

[19] Eresen A, Sun C, Zhou K, Shangguan J, Wang B, Pan L, Hu S, Ma Q, Yang J, Zhang Z and Yaghmai V. Early differentiation of irreversible electroporation ablation regions with radiomics features of conventional MRI. *Acad Radiol* 2021; [Epub ahead of print].

## Early detection IRE ablation response for liver tumor

- [20] Kononenko I, Šimec E and Robnik-Šikonja M. Overcoming the myopia of inductive learning algorithms with RELIEFF. *Appl Intell* 1997; 7: 39-55.
- [21] Eresen A, Yang J, Scotti A, Cai K, Yaghmai V and Zhang Z. Combination of natural killer cell-based immunotherapy and irreversible electroporation for the treatment of hepatocellular carcinoma. *Ann Transl Med* 2021; 9: 1089.
- [22] Vroomen LGPH, Scheffer HJ, Melenhorst MCAM, de Jong MC, van den Bergh JE, van Kuijk C, van Delft F, Kazemier G and Meijerink MR. MR and CT imaging characteristics and ablation zone volumetry of locally advanced pancreatic cancer treated with irreversible electroporation. *Eur Radiol* 2017; 27: 2521-2531.
- [23] Akinwande O, Ahmad SS, Van Meter T, Schulz B and Martin RCG. CT findings of patients treated with irreversible electroporation for locally advanced pancreatic cancer. *J Oncol* 2015; 2015: 680319.
- [24] Wile GE, Leyendecker JR, Krehbiel KA, Dyer RB and Zagoria RJ. CT and MR imaging after imaging-guided thermal ablation of renal neoplasms. *Radiographics* 2007; 27: 325-339.
- [25] Hsiao CY and Huang KW. Irreversible electroporation: a novel ultrasound-guided modality for non-thermal tumor ablation. *J Med Ultrasound* 2017; 25: 195-200.
- [26] Schmidt CR, Shires P and Mootoo M. Real-time ultrasound imaging of irreversible electroporation in a porcine liver model adequately characterizes the zone of cellular necrosis. *HPB (Oxford)* 2012; 14: 98-102.
- [27] Zhou L, Yin S, Chai W, Zhao Q, Tian G, Xu D and Jiang Ta. Irreversible electroporation in patients with liver tumours: treated-area patterns with contrast-enhanced ultrasound. *World J Surg Oncol* 2020; 18: 305.
- [28] Wang X, Su Z, Lyu T, Figini M, Procissi D, Shang-guan J, Sun C, Wang B, Shang N, Gu S, Ma Q, Gordon AC, Lin K, Wang J, Lewandowski RJ, Salem R, Yaghmai V, Larson AC and Zhang Z. 18F-FDG PET biomarkers help detect early metabolic response to irreversible electroporation and predict therapeutic outcomes in a rat liver tumor model. *Radiology* 2018; 287: 137-145.
- [29] Meijerink MR, Ruarus AH, Vroomen LGPH, Puijk RS, Geboers B, Nieuwenhuizen S, van den Bemd BAT, Nielsen K, de Vries JJJ, van Lienden KP, Lissenberg-Witte BI, van den Tol MP and Scheffer HJ. Irreversible electroporation to treat unresectable colorectal liver metastases (COLDFIRE-2): a phase II, two-center, single-arm clinical trial. *Radiology* 2021; 299: 470-480.
- [30] Guo Y, Zhang Y, Klein R, Nijm GM, Sahakian AV, Omary RA, Yang GY and Larson AC. Irreversible electroporation therapy in the liver: longitudinal efficacy studies in a rat model of hepatocellular carcinoma. *Cancer Res* 2010; 70: 1555-1563.
- [31] Sánchez-Velázquez P, Castellví Q, Villanueva A, Iglesias M, Quesada R, Pañella C, Cáceres M, Dorcaratto D, Andaluz A, Moll X, Burdío JM, Grande L, Ivorra A and Burdío F. Long-term effectiveness of irreversible electroporation in a murine model of colorectal liver metastasis. *Sci Rep* 2017; 7: 44821.
- [32] Varghese BA, Cen SY, Hwang DH and Duddalwar VA. Texture analysis of imaging: what radiologists need to know. *AJR Am J Roentgenol* 2019; 212: 520-528.
- [33] Rajkomar A, Dean J and Kohane I. Machine learning in medicine. *N Engl J Med* 2019; 380: 1347-1358.
- [34] Eresen A, Yang J, Shangguan J, Li Y, Hu S, Sun C, Yaghmai V, Benson Iii AB and Zhang Z. Prediction of therapeutic outcome and survival in a transgenic mouse model of pancreatic ductal adenocarcinoma treated with dendritic cell vaccination or CDK inhibitor using MRI texture: a feasibility study. *Am J Transl Res* 2020; 12: 2201-2211.
- [35] Kim J, Min JH, Kim SK, Shin SY and Lee MW. Detection of hepatocellular carcinoma in contrast-enhanced magnetic resonance imaging using deep learning classifier: a multi-center retrospective study. *Sci Rep* 2020; 10: 9458.

## Early detection IRE ablation response for liver tumor

**Supplementary Table 1.** List of quantitative imaging features

Feature type	Feature extraction method	Descriptions	
Intensity	FOS: First order statistics	Mean	
		Standard deviation	
		Third moment	
		Entropy	
		Kurtosis	
Texture	Co-occurrence matrix features	Skewness	
		Energy	
		Contrast	
		Entropy	
		Homogeneity	
		Correlation	
		Sum average	
		Variance	
		Dissimilarity	
		Autocorrelation	
		Run-length matrix features	Short-run emphasis
			Long run emphasis
			Gray-level nonuniformity
			Run length nonuniformity
			Run percentage
	Low gray-level run emphasis		
	High gray-level run emphasis		
	Short-run low gray-level emphasis		
	Short-run high gray-level emphasis		
	Long run low gray-level emphasis		
	Long run high gray-level emphasis		
	Gray-level variance		
	Size-zone matrix features	Run-length variance	
		Small zone emphasis	
		Large zone emphasis	
		Gray-level nonuniformity	
		Zone-size nonuniformity	
		Zone percentage	
		Low gray-level zone emphasis	
		High gray-level zone emphasis	
		Small zone low gray-level emphasis	
		Small zone high gray-level emphasis	
		Large zone low gray-level emphasis	
Large zone high gray-level emphasis			
Neighborhood gray-tone-difference matrix features	Gray-level variance		
	Zone-size variance		
	Coarseness		
	Contrast		
	Busyness		
		Complexity	
		Strength	

## Early detection IRE ablation response for liver tumor

**Supplementary Table 2.** List of the selected candidate features

Model	Feature extraction method	Description
T1w MRI	FoS	Kurtosis
	RLM	Long run high gray-level emphasis
	RLM	Long run emphasis
	RLM	Run-length variance
	SZM	Zone-size variance
	SZM	Large zone low gray-level emphasis
	SZM	Small zone high gray-level emphasis
	SZM	Small zone emphasis
	SZM	Small zone low gray-level emphasis
	TDM	Busyness
T2w MRI	FoS	Kurtosis
	RLM	Long run low gray-level emphasis
	RLM	Gray-level nonuniformity
	RLM	Long run high gray-level emphasis
	SZM	Zone-size variance
	SZM	Gray-level nonuniformity
	SZM	Small zone low gray-level emphasis
	TDM	Coarseness
	TDM	Strength
	TDM	Busyness
T1w + T2w MRI	TDM	Busyness
	FoS <sup>2</sup>	Kurtosis
	RLM <sup>1</sup>	Long run emphasis
	RLM <sup>1</sup>	Long run high gray-level emphasis
	RLM <sup>2</sup>	Gray-level nonuniformity
	SZM <sup>1</sup>	Zone-size variance
	SZM <sup>1</sup>	Large zone low gray-level emphasis
	SZM <sup>2</sup>	Zone-size variance
	SZM <sup>2</sup>	Gray-level nonuniformity
	TDM <sup>1</sup>	Busyness
TDM <sup>2</sup>	Busyness	

<sup>1</sup>The features were computed from T1w MRI data. <sup>2</sup>The features were computed from T2w MRI data.